



Article

# Rectifying Nonreciprocal Perfect Absorber Based on Generalized Effective-Medium Theory for Composite Magnetic Metamaterials

Yiyun Chen <sup>1</sup>, Yaping Zhang <sup>1</sup>, Lingzhong Zhao <sup>1</sup>, Guangfeng Wen <sup>1</sup>, Lin Zhang <sup>1</sup>, Qingtao Ba <sup>1,2</sup>, Qilin Luo <sup>1,3</sup>, Jingjing Yu <sup>1</sup> and Shiyang Liu <sup>1,\*</sup><sup>1</sup> Key Laboratory of Optical Information Detecting and Display Technology, Zhejiang Normal University, Jinhua 321004, China<sup>2</sup> Department of Physics and Institute of Electromagnetics and Acoustics, Xiamen University, Xiamen 361005, China<sup>3</sup> Xiangsihu College, Guangxi University for Nationalities, Nanning 530225, China

\* Correspondence: syliu@zjnu.cn

**Abstract:** In this work, we demonstrate the implementation of a nonreciprocal perfect absorber (NPA) made of composite magnetic metamaterials (MMs) consisting of an array of dielectric core loaded (DCL) ferrite rods with either hollow or dielectric cores. The NPA can be functionalized as a PA for the incident beam at a specified direction, while at the symmetric direction the absorption is very weak so that a strong reflection is observed due to the excitation of nonreciprocal magnetic surface plasmon. Interestingly, it is shown that the material loss might be beneficial to the absorption, but it will result in the degradation of nonreciprocal performance. For the delicately designed MMs, only a very small material loss is necessary and simultaneously ensures the high nonreciprocal performance of NPA. To interpret the high quality of NPA, we developed a generalized effective-medium theory for the composite MMs, which shows the direct consequence of the DCL ferrite rods with optimized core size and core permittivity. The partial wave analysis indicates that the nonreciprocal dipole resonance in DCL ferrite rod plays a crucial role in improving the nonreciprocity. The narrow band feature and the angular sensitivity make the NPA promising for the diode-like functionalities. In addition, by controlling the magnitude and orientation of bias magnetic field both the operating frequency and the nonreciprocity can be flexibly controlled, adding an additional degree of freedom. The concept proposed in this research is promising for microwave photonics and integrated photonics.

**Keywords:** nonreciprocal perfect absorber; magnetic metamaterials; magnetic surface plasmon; time-reversal symmetry breaking; effective-medium theory; multiple scattering theory



**Citation:** Chen, Y.; Zhang, Y.; Zhao, L.; Wen, G.; Zhang, L.; Ba, Q.; Luo, Q.; Yu J.; Liu, S. Rectifying Nonreciprocal Perfect Absorber Based on Generalized Effective-Medium Theory for Composite Magnetic Metamaterials. *Photonics* **2022**, *9*, 699. <https://doi.org/10.3390/photonics9100699>

Received: 31 August 2022

Accepted: 23 September 2022

Published: 27 September 2022

**Publisher's Note:** MDPI stays neutral with regard to jurisdictional claims in published maps and institutional affiliations.



**Copyright:** © 2022 by the authors. Licensee MDPI, Basel, Switzerland. This article is an open access article distributed under the terms and conditions of the Creative Commons Attribution (CC BY) license (<https://creativecommons.org/licenses/by/4.0/>).

## 1. Introduction

Material loss is an inevitable issue in designing metamaterials or metasurfaces, which is usually detrimental to the performance of most functionalities, limiting severely the potential applications. Nonetheless, material loss is indispensable and plays a positive role in designing the absorber as is certain. Traditional absorbers are usually made of materials with either large dielectric loss or large magnetic loss and in form of pyramidal absorber, tapered absorber, or laminated absorber [1–5], which apparently suffer from bulky geometry, frequency limitation, and lack of appropriate materials. The advancement of nanotechnology enables the fabrication of nanomaterials with unique structures, which exhibits particular absorption features such as the broadband and nearly omnidirectional absorber by the biomimetic silicon nanostructures [6], a low index super black absorber by the vertically aligned carbon nanotube arrays [7], an impedance-graded absorber by layered aluminum [8], and other chemical synthesis nanomaterial absorbers achieved by amplified interface effects [9–12]. Nonetheless, the absorbing characteristics of these

nanomaterials mainly depends on the material property in itself, thus limiting the flexibility in practical applications.

The advent of metamaterials and metasurfaces provides a new concept in designing electromagnetic media, which, in principle, can create arbitrary electric and magnetic response. Initiated by the pioneering work from Padilla and coworkers [13,14], a variety of metamaterial or metasurface based perfect absorbers (PAs) come into appearance, including the dual-band absorbers [15–18], the multi-band absorbers [19–22], and the broadband absorbers [23–26]; the polarization-dependent absorbers [27–30] and the polarization-independent absorbers [31–34]; the wide angle [35–38] and even omnidirectional absorbers [25,31,39,40]. Due to the sufficient properties of these sub-wavelength structured absorbers, many potential and promising applications have been demonstrated such as photovoltaics [41–43], photodetectors [44–46], photocatalysis [47–49], bolometers [50–52], biosensors [53–55], imaging sensors [56–58], thermal emitters [59–61], and spatial light modulators [62–64]. In addition, the PAs have also been implemented in the optical systems with extraordinary physical properties, for instance, the coherent perfect absorption, a time-reversal counterpart of laser emission process [65], can be achieved in metamaterial based systems [66,67]. By engineering parity-time symmetry phase in metamaterials, the PAs can be achieved, showing significant contribution to the non-Hermitian photonics [68–70]. Zero-index materials, especially, epsilon-near-zero materials can be served as a candidate to construct PAs due to the enhancement of light-matter interaction [71–74]. Interestingly, based on the gradient index system, termed photonic “black hole” [75,76], the omnidirectional PAs are shown to effectively trap light by mimicking celestial mechanics [77,78]. For the metasurfaces made up of high-Q resonator arrays, quasibound states in the continuum emerge and result in the realization of narrow-band PAs, triggering potential applications in photodetection and sensing [79–81]. By introducing nonlinear dielectric inclusions, the nonlinear PAs can be constructed with intensity-dependent absorption features, extending the possible applications to nonlinear optics [82–84]. Besides, the concept of metamaterial or metasurface based PAs is also applicable for acoustic waves so that the airborne and underwater acoustic PAs are theoretically proposed and experimentally realized [85–88].

To gain more degrees of freedom, the PAs with properties controllable by external stimuli are preferred by incorporating active materials into the design of metamaterials or metasurfaces. It has been shown that several choices can meet the requirement in dynamically modulating the electromagnetic performance, including the liquid crystal based metamaterial PAs electronically tuned by a bias voltage [89–91], the 2D materials, especially, graphene, used as either patterned or unpatterned film in metamaterials or metasurfaces, showing the tunable properties by controlling Fermi level via a bias voltage [18,37,92], and the phase-change materials such as  $\text{Ge}_2\text{Sb}_2\text{Te}_5$  and  $\text{VO}_2$ , possessing, respectively, amorphous to crystalline and insulating to metallic phase transition, determined by thermal process, exhibiting reconfigurable properties for the associated metamaterials or metasurfaces [32,63,93–96]. Besides, by combining micro-electromechanical systems with PAs the mechanically tunable functionalities can be achieved with the operating frequency flexibly controlled by precisely adjusting the configurations [97–99]. Ferrite materials, as an important stuff in microwave engineering, can be served as another candidate to implement tunable electromagnetic functionalities due to the dependence of magnetic permeability on a bias magnetic field (BMF). By constructing magnetic metamaterials (MMs) with an array of ferrite rods, the corresponding effective refractive index can be tuned from negative to zero and to positive with a BMF [100–102]. In addition, due to the introduction of BMF the time-reversal symmetry is broken, giving rise to nonreciprocal features of MMs, such as nonreciprocal scattering [103,104], nonreciprocal waveguiding [105–107], and nonreciprocal edge modes [108–110]. In addition, magnetic surface plasmon (MSP) can be excited in MMs due to the intrinsic magnetic response of ferrite materials [111], which is a magnetic counterpart of electric surface plasmon in metallic materials. Differently, the MSP resonance can be flexibly tuned in that the operating frequency and the nonreciprocity can

be controlled, respectively, by the magnitude and direction of a BMF. In this work, we find that the loss in MMs can induce nonreciprocal absorption or reflection, while strong loss will degrade the nonreciprocal effect. Our motivation is to find the optimal material loss and enhance the nonreciprocity of MMs, namely, for the electromagnetic beam incident from one direction the field is completely absorbed, corresponding to the PA, while the electromagnetic beam is nearly totally reflected when it strikes the MMs at a mirror-symmetric direction. To achieve this purpose, the composite MMs made up of an array of delicately optimized dielectric core loaded (DCL) ferrite rods are constructed, instead of the MMs consisting of pure ferrite rods. Based on the retrieved effective constitutive parameters from the generalized effective-medium theory and the partial wave maps simulated by the multiple scattering theory, the phenomenon can be perfectly interpreted. In addition, the introduction of DCL ferrite rods can induce another resonating mode residing in the interior region associated with the angular momentum channel  $n = -1$ , substantially different from the  $n = +1$  mode emerging in the exterior region. As a result, the nonreciprocal dipole modes are constituted, which can remarkably improve the quality of nonreciprocity.

## 2. Effective-Medium Theory

Ferrite materials, typically, yttrium iron garnets (YIGs) are widely used in microwave engineering, which have different electromagnetic parameters dependent on the material elements, the concentrations, and the crystal type as single-crystalline or poly-crystalline phase. The electric permittivity of YIG is usually very large and it does not change too much for the YIG ferrite materials with different elements and concentrations. In addition, the permittivity is not a critical parameter that determines the nonreciprocal perfect absorbing effect. Therefore, we take  $\epsilon_s = 15 + i3 \times 10^{-3}$  as a constant for the convenience of theoretical exploration although it is not a rigorous treatment. The damping factor  $\alpha$ , associated with the linewidth of gyromagnetic resonance, varies in a wide range, which is beneficial to the loss optimization. Under fully magnetization by a BMF along  $z$  axis, the magnetic permeability is a second-order tensor in gyrotropic form [112]

$$\hat{\mu} = \mu_s \begin{pmatrix} \mu_r & -i\mu_\kappa & 0 \\ i\mu_\kappa & \mu_r & 0 \\ 0 & 0 & 1 \end{pmatrix}, \quad \mu_s \hat{\mu}^{-1} = \begin{pmatrix} \mu'_r & -i\mu'_\kappa & 0 \\ i\mu'_\kappa & \mu'_r & 0 \\ 0 & 0 & 1 \end{pmatrix} \quad (1)$$

with

$$\mu_r = 1 + \frac{\omega_m(\omega_0 - i\alpha\omega)}{(\omega_0 - i\alpha\omega)^2 - \omega^2}, \quad \mu'_r = \frac{\mu_r}{\mu_r^2 - \mu_\kappa^2}, \quad \mu_\kappa = \frac{-\omega_m\omega}{(\omega_0 - i\alpha\omega)^2 - \omega^2}, \quad \mu'_\kappa = \frac{-\mu_\kappa}{\mu_r^2 - \mu_\kappa^2},$$

where  $\omega$  is the circular frequency of the incident electromagnetic wave,  $\alpha$  is the damping factor,  $\omega_0 = 2\pi f_0 = 2\pi\gamma H_0$  is the ferromagnetic resonance frequency with  $H_0$  the BMF and  $\gamma = 2.8$  MHz/Oe the gyromagnetic ratio,  $\omega_m = 2\pi f_m = 2\pi\gamma M_s$  is the characteristic frequency with  $M_s$  is the saturation magnetization, set  $M_s = 1750$  G for the convenience of analysis. In two dimensional system, only the transverse magnetic (TM) electromagnetic waves with the electric field component polarized along  $z$  direction interact with magnetic moment. To illustrate this, the geometry of a ferrite rod positioned in air background illuminated by an electromagnetic wave of TM polarization is shown in Figure 1a, where both electric field and BMF are along  $z$  axis. The ferrite rod has the radius  $r_s$  and the dielectric core has the radius  $r_c$  and the permittivity  $\epsilon_c$ , the permeability  $\mu_c = 1$  or, even simpler,  $\epsilon_c = \mu_c = 1$  for hollow ferrite rod. The composite MM is constructed by an array of DCL ferrite rods arranged periodically in the air as schematically shown in Figure 1b, where a square lattice with the lattice separation  $a$  is considered.

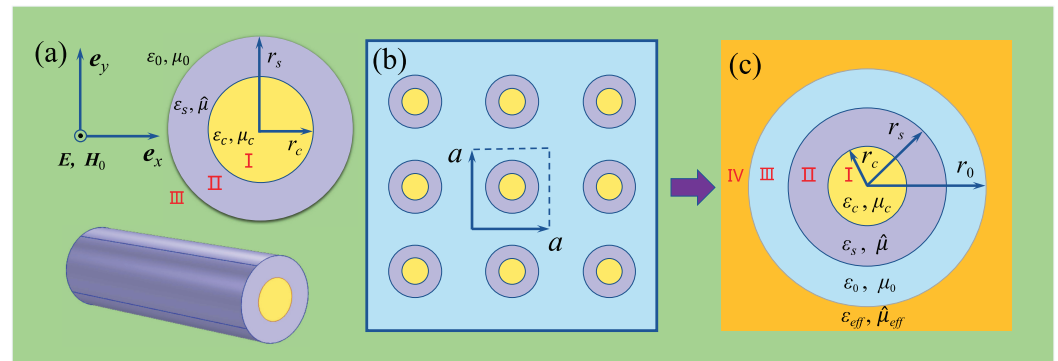


**Figure 1.** The schematic diagram illustrating the geometry of a DCL ferrite rod in air background under the illumination of an electromagnetic wave with TM polarization (a), the composite MM made up of an array of DCL ferrite rods arranged periodically as a square lattice in the air (b), as well as the transformation of a unit cell in panel (b) into a TL hybrid rod (c) in effective-medium theory.

The concept of effective-medium theory (EMT) is based on the coherent potential approximation, which has been applied to retrieve the effective constitutive parameters for the dielectric metamaterials [113] and MMs made of pure ferrite rods [114]. To generalize the EMT to the composite MMs concerned in present work, it is supposed that the composite MMs possess the effective electric permittivity  $\epsilon_{eff}$  and effective magnetic permeability  $\mu_{eff}$ . Then, as schematically shown in Figure 1c, the unit cell is transformed into an equal-area three-layer (TL) hybrid rod with the inner part the DCL ferrite rod and the outmost layer the background medium, namely, the air in present case. Immersed this TL hybrid rod into the effective medium, the scattering cross section should be zero, which is the criterion to establish the necessary formulae so that the effective constitutive parameters can be acquired. Based on the Mie theory, the scattering properties of a TL hybrid rod can be solved exactly, which involves the expansion of electromagnetic wave in four regions I, II, III, IV into vector cylindrical wave functions (VCWFs) at first step. As a result, the electromagnetic field in region I, corresponding to the dielectric core, can be written as

$$E_1 = \sum_n E_n q_n^1 N_n^{(1)}(k_c, r), \tag{2a}$$

$$H_1 = \frac{k_c}{i\omega\mu_0\mu_c} \sum_n E_n q_n^1 M_n^{(1)}(k_c, r), \tag{2b}$$

where the coefficient  $E_n = i^n |E_0|$  with  $|E_0|$  the amplitude of electromagnetic waves,  $q_n^1$  are the corresponding expansion coefficients, and the wave number in region I is  $k_c = k_0 \sqrt{\epsilon_c \mu_c}$  with  $k_0$  the wave number in vacuum. Then, in region II, corresponding to the ferrite material, the electromagnetic waves are expanded into VCWFs as

$$E_2 = \sum_n E_n \left[ q_n^2 N_n^{(1)}(k'_s, r) - b_n^2 N_n^{(3)}(k'_s, r) \right], \tag{3a}$$

$$H_2 = \frac{k'_s}{i\omega\mu_0} \sum_n E_n \left\{ q_n^2 \left[ \mu'_r M_n^{(1)}(k'_s, r) + i\mu'_k L_n^{(1)}(k'_s, r) \right] - b_n^2 \left[ \mu'_r M_n^{(3)}(k'_s, r) + i\mu'_k L_n^{(3)}(k'_s, r) \right] \right\}, \tag{3b}$$

where  $q_n^2$  and  $b_n^2$  are the corresponding expansion coefficients, the effective wave number in region II is  $k'_s = k_0 \frac{\sqrt{\epsilon_s} \sqrt{\mu_s}}{\sqrt{\mu_0} \sqrt{\mu'_r}}$ . In usual case,  $\mu_s = \mu_0$  such that  $k'_s = k_0 \frac{\sqrt{\epsilon_s}}{\sqrt{\mu'_r}}$ . Similarly, in region III the electromagnetic wave can be expanded as

$$\mathbf{E}_3 = \sum_n E_n \left[ q_n^3 \mathbf{N}_n^{(1)}(k_0, \mathbf{r}) - b_n^3 \mathbf{N}_n^{(3)}(k_0, \mathbf{r}) \right], \tag{4a}$$

$$\mathbf{H}_3 = \frac{k_0}{i\omega\mu_0} \sum_n E_n \left[ q_n^3 \mathbf{M}_n^{(1)}(k_0, \mathbf{r}) - b_n^3 \mathbf{M}_n^{(3)}(k_0, \mathbf{r}) \right], \tag{4b}$$

where  $q_n^3$  and  $b_n^3$  are the corresponding expansion coefficients. Finally, for the effective-medium background in region IV, it is actually a new ferrite materials with the electromagnetic properties dependent on the configuration of composite MMs. As a result, the electromagnetic wave can be easily expanded by replacing  $k'_s$ ,  $\mu'_r$ , and  $\mu'_k$  in Equation (3) with the effective parameters  $k_e$ ,  $\mu'_{re}$ , and  $\mu'_{ke}$ , which are to be obtained in the following part.

$$\mathbf{E}_4 = \sum_n E_n \left[ q_n^4 \mathbf{N}_n^{(1)}(k_e, \mathbf{r}) - b_n^4 \mathbf{N}_n^{(3)}(k_e, \mathbf{r}) \right], \tag{5a}$$

$$\mathbf{H}_4 = \frac{k_e}{i\omega\mu_0} \sum_n E_n \left\{ q_n^4 \left[ \mu'_{re} \mathbf{M}_n^{(1)}(k_e, \mathbf{r}) + i\mu'_{ke} \mathbf{L}_n^{(1)}(k_e, \mathbf{r}) \right] - b_n^4 \left[ \mu'_{re} \mathbf{M}_n^{(3)}(k_e, \mathbf{r}) + i\mu'_{ke} \mathbf{L}_n^{(3)}(k_e, \mathbf{r}) \right] \right\}, \tag{5b}$$

where the effective wave number in the homogenized composite MMs is  $k_e = k_0 \frac{\sqrt{\epsilon_{eff}}}{\sqrt{\mu'_{re}}}$ , or, in a more convenient form  $k_e = k_0 \sqrt{\epsilon_{eff}} \sqrt{\mu_{eff}}$ . The VCWFs  $\mathbf{L}_n^{(J)}$ ,  $\mathbf{M}_n^{(J)}$ , and  $\mathbf{N}_n^{(J)}$  used in the above formulae are defined as

$$\mathbf{L}_n^{(J)}(k, \mathbf{r}) = \left[ \frac{dz_n^{(J)}(x)}{dx} \mathbf{e}_r + \frac{in}{x} z_n^{(J)}(x) \mathbf{e}_\phi \right] e^{in\phi}, \tag{6a}$$

$$\mathbf{M}_n^{(J)}(k, \mathbf{r}) = \left[ \frac{in}{x} z_n^{(J)}(x) \mathbf{e}_r - \frac{dz_n^{(J)}(x)}{dx} \mathbf{e}_\phi \right] e^{in\phi}, \tag{6b}$$

$$\mathbf{N}_n^{(J)}(k, \mathbf{r}) = z_n^{(J)}(x) e^{in\phi} \mathbf{e}_z, \tag{6c}$$

where  $x = kr$ , the superscript  $J = 1$  and  $J = 3$  in  $z_n^{(J)}(x)$  correspond to the Bessel function  $J_n(x)$  and the first kind Hankel function  $H_n^{(1)}(x)$ , respectively.

By matching boundary conditions at three interfaces  $r = r_c$ ,  $r = r_s$ , and  $r = r_0$

$$\mathbf{E}_1 \times \mathbf{e}_r|_{r_c} = \mathbf{E}_2 \times \mathbf{e}_r|_{r_c}, \quad \mathbf{H}_1 \times \mathbf{e}_r|_{r_c} = \mathbf{H}_2 \times \mathbf{e}_r|_{r_c}, \tag{7a}$$

$$\mathbf{E}_2 \times \mathbf{e}_r|_{r_s} = \mathbf{E}_3 \times \mathbf{e}_r|_{r_s}, \quad \mathbf{H}_2 \times \mathbf{e}_r|_{r_s} = \mathbf{H}_3 \times \mathbf{e}_r|_{r_s}, \tag{7b}$$

$$\mathbf{E}_3 \times \mathbf{e}_r|_{r_0} = \mathbf{E}_4 \times \mathbf{e}_r|_{r_0}, \quad \mathbf{H}_3 \times \mathbf{e}_r|_{r_0} = \mathbf{H}_4 \times \mathbf{e}_r|_{r_0}, \tag{7c}$$

we can obtain the corresponding linear equations as follows

$$q_n^1 J_n(k_c r_c) = q_n^2 J_n(k'_s r_c) - b_n^2 H_n^{(1)}(k'_s r_c), \tag{8a}$$

$$\frac{k_c}{i\omega\mu_0\mu_c} q_n^1 J'_n(k_c r_c) = \frac{k'_s}{i\omega\mu_0} \left[ q_n^2 \tilde{J}_n(k'_s r_c) - b_n^2 \tilde{H}_n(k'_s r_c) \right], \tag{8b}$$

$$q_n^2 J_n(k'_s r_s) - b_n^2 H_n^{(1)}(k'_s r_s) = q_n^3 J_n(k_0 r_s) - b_n^3 H_n^{(1)}(k_0 r_s), \tag{8c}$$

$$\frac{k'_s}{i\omega\mu_0} \left[ q_n^2 \tilde{J}_n(k'_s r_s) - b_n^2 \tilde{H}_n^{(1)}(k'_s r_s) \right] = \frac{k_0}{i\omega\mu_0} \left[ q_n^3 J'_n(k_0 r_s) - b_n^3 H_n^{(1)'}(k_0 r_s) \right], \tag{8d}$$

$$q_n^3 J_n(k_0 r_0) - b_n^3 H_n^{(1)}(k_0 r_0) = q_n^4 J_n(k_e r_0) - b_n^4 H_n^{(1)}(k_e r_0), \tag{8e}$$

$$\frac{k_0}{i\omega\mu_0} \left[ q_n^3 J'_n(k_0 r_0) - b_n^3 H_n^{(1)'}(k_0 r_0) \right] = \frac{k_e}{i\omega\mu_0} \left[ q_n^4 \bar{J}_n(k_e r_0) - b_n^4 \bar{H}_n(k_e r_0) \right], \tag{8f}$$

where the functions  $\tilde{J}_n(x), \bar{J}_n(x)$  are associated with the Bessel function and the functions  $\tilde{H}_n(x), \bar{H}_n(x)$  are associated with the Hankel function of the first kind, which are defined as

$$\tilde{J}_n(x) = \mu'_r J'_n(x) + \frac{n\mu'_k}{x} J_n(x), \quad \bar{J}_n(x) = \mu'_{re} J'_n(x) + \frac{n\mu'_{ke}}{x} J_n(x), \tag{9a}$$

$$\tilde{H}_n(x) = \mu'_r H_n^{(1)'}(x) + \frac{n\mu'_k}{x} H_n^{(1)}(x), \quad \bar{H}_n(x) = \mu'_{re} H_n^{(1)'}(x) + \frac{n\mu'_{ke}}{x} H_n^{(1)}(x). \tag{9b}$$

By solving the first four linear equations, namely, Equation (8a–d), the Mie coefficients for the DCL ferrite rod in the background of composite MMs in Figure 1 can be obtained.

$$\mathcal{T}_n = \frac{b_n^3}{q_n^3} = \frac{k_0 J'_n(k_0 r_s) \Xi(k'_s r_s) - k'_s J_n(k_0 r_s) \tilde{\Xi}(k'_s r_s)}{k_0 H_n^{(1)'}(k_0 r_s) \Xi(k'_s r_s) - k'_s H_n^{(1)}(k_0 r_s) \tilde{\Xi}(k'_s r_s)}, \tag{10}$$

where the functions  $\Xi(k'_s r_s)$  and  $\tilde{\Xi}(k'_s r_s)$  are the formulae in connection to the scattering properties at the innermost interface  $r = r_c$  and they are defined as

$$\Xi(k'_s r_s) = J_n(k'_s r_s) - \mathcal{R}_n H_n^{(1)}(k'_s r_s), \quad \tilde{\Xi}(k'_s r_s) = \tilde{J}_n(k'_s r_s) - \mathcal{R}_n \tilde{H}_n(k'_s r_s), \tag{11}$$

in which the scattering term  $\mathcal{R}_n$  is defined as

$$\mathcal{R}_n = \frac{b_n^2}{q_n^2} = \frac{\tilde{J}_n(k'_s r_c) J_n(k_c r_c) - \tilde{k} J_n(k'_s r_c) J'_n(k_c r_c)}{\tilde{H}_n(k'_s r_c) J_n(k_c r_c) - \tilde{k} H_n^{(1)}(k'_s r_c) J'_n(k_c r_c)}, \tag{12}$$

with the normalized dimensionless wave number  $\tilde{k} = \frac{k_c}{k'_s \mu_c}$ .

With the Mie coefficients of the DCL ferrite rod at hand, we can further consider the scattering properties of TL hybrid rod immersed in the effective medium. Note in passing that the scattering cross section tends to be zero as required by the effective-medium theory, which can substantially simplify the problem. Provided that the Mie coefficients of the TL hybrid rod is  $\mathcal{S}_n$ , the scattering cross section of the TL hybrid rod can be acquired according to the Mie theory [113].

$$C_{sca} = \frac{4}{k_e} \sum_n |\mathcal{S}_n|^2 = \frac{4}{k_e} \sum_n \left| \frac{b_n^4}{q_n^4} \right|^2 = 0. \tag{13}$$

As a consequence, the expansion coefficients in region IV should be vanished, namely,  $b_n^4 = 0$ . With the aid of this judgement and combined with the obtained Mie coefficients  $\mathcal{T}_n$  of the DCL ferrite rod in Equation (10), the master equation of effective-medium theory

can be obtained by solving boundary equations, namely, Equations (8e) and (8f), which is written as

$$\mathcal{T}_n = \frac{n\mu'_{ke}J_n(x_0)J_n(x_e) + x_e\mu'_{re}J_n(x_0)J'_n(x_e) - x_0J'_n(x_0)J_n(x_e)}{n\mu'_{ke}H_n^{(1)}(x_0)J_n(x_e) + x_e\mu'_{re}H_n^{(1)}(x_0)J'_n(x_e) - x_0H_n^{(1)'}(x_0)J_n(x_e)}, \quad (14)$$

where the size parameters  $x_0 = k_0r_0$  and  $x_e = k_er_0$ . In the long wavelength limit, only the lower order terms contribute to the scattering cross section so that the angular momentum channels  $n = 0, \pm 1$  are taken into account in effective-medium theory, giving rise to the following three equations

$$\mathcal{T}_0 = \frac{x_e\mu'_{re}J_0(x_0)J'_0(x_e) - x_0J'_0(x_0)J_0(x_e)}{x_e\mu'_{re}H_0^{(1)}(x_0)J'_0(x_e) - x_0H_0^{(1)'}(x_0)J_0(x_e)}, \quad (15a)$$

$$\mathcal{T}_{+1} = \frac{\mu'_{ke}J_1(x_0)J_1(x_e) + x_e\mu'_{re}J_1(x_0)J'_1(x_e) - x_0J'_1(x_0)J_1(x_e)}{\mu'_{ke}H_1^{(1)}(x_0)J_1(x_e) + x_e\mu'_{re}H_1^{(1)}(x_0)J'_1(x_e) - x_0H_1^{(1)'}(x_0)J_1(x_e)}, \quad (15b)$$

$$\mathcal{T}_{-1} = \frac{x_e\mu'_{re}J_1(x_0)J'_1(x_e) - \mu'_{ke}J_1(x_0)J_1(x_e) - x_0J'_1(x_0)J_1(x_e)}{x_e\mu'_{re}H_1^{(1)}(x_0)J'_1(x_e) - \mu'_{ke}H_1^{(1)}(x_0)J_1(x_e) - x_0H_1^{(1)'}(x_0)J_1(x_e)}. \quad (15c)$$

In the effective-medium theory, the unit cell is transformed into an equal-area TL hybrid rod with the radius  $r_0 = a/\sqrt{\pi}$  for the square lattice shown in Figure 1b. As a matter of fact, the long wavelength requirement of effective-medium theory indicates that  $k_er_0 \ll 1$  to guarantee the homogenization of the composite MMs. Therefore, Equations (15a)–(15c) can be evidently simplified by making approximations on  $J_n(x)$ ,  $J'_n(x)$ ,  $H_n^{(1)}(x)$ , and  $H_n^{(1)'}(x)$ , concretely,

$$J_0(x) \simeq 1, \quad J_1(x) \simeq \frac{x}{2}, \quad (16a)$$

$$J'_0(x) \simeq -\frac{x}{2}, \quad J'_1(x) \simeq \frac{1}{2}, \quad (16b)$$

$$H_0^{(1)}(x) \simeq 1 + \frac{2i}{\pi} \ln x, \quad H_1^{(1)}(x) \simeq \frac{x}{2} - \frac{2i}{\pi x}, \quad (16c)$$

$$H_0^{(1)'}(x) \simeq -\frac{x}{2} + \frac{2i}{\pi x}, \quad H_1^{(1)'}(x) \simeq \frac{1}{2} + \frac{2i}{\pi x^2}. \quad (16d)$$

Substituting these terms into Equations (15a)–(15c), the master equations can be transformed into the solvable linear equations

$$\mathcal{T}_0 = \frac{x_e^2\mu'_{re}J_0(x_0) + 2x_0J'_0(x_0)}{x_e^2\mu'_{re}H_0^{(1)}(x_0) + 2x_0H_0^{(1)'}(x_0)}, \quad (17a)$$

$$\mathcal{T}_{+1} = \frac{\mu'_{ke}J_1(x_0) + \mu'_{re}J_1(x_0) - x_0J'_1(x_0)}{\mu'_{ke}H_1^{(1)}(x_0) + \mu'_{re}H_1^{(1)}(x_0) - x_0H_1^{(1)'}(x_0)}, \quad (17b)$$

$$\mathcal{T}_{-1} = \frac{\mu'_{re}J_1(x_0) - \mu'_{ke}J_1(x_0) - x_0J'_1(x_0)}{\mu'_{re}H_1^{(1)}(x_0) - \mu'_{ke}H_1^{(1)}(x_0) - x_0H_1^{(1)'}(x_0)}. \quad (17c)$$

After some simple mathematical manipulations, we finally obtain the effective constitutive parameters, namely,  $\epsilon_{eff}$ ,  $\mu'_{re}$ , and  $\mu'_{ke}$

$$\epsilon_{eff} = \frac{2}{x_0} \frac{J'_0(x_0) - \mathcal{T}_0 H_0^{(1)'}(x_0)}{\mathcal{T}_0 H_0^{(1)}(x_0) - J_0(x_0)}, \tag{18a}$$

$$\mu'_{re} = \frac{x_0}{2} \frac{2\mathcal{T}_{+1}\mathcal{T}_{-1}\Pi_1 - (\mathcal{T}_{+1} + \mathcal{T}_{-1})(\Pi_2 + \Pi_3) + 2\Pi_4}{[\mathcal{T}_{-1}H_1^{(1)}(x_0) - J_1(x_0)][\mathcal{T}_{+1}H_1^{(1)}(x_0) - J_1(x_0)]}, \tag{18b}$$

$$\mu'_{ke} = \frac{x_0}{2} \frac{(\mathcal{T}_{+1} - \mathcal{T}_{-1})(\Pi_3 - \Pi_2)}{[J_1(x_0) - \mathcal{T}_{+1}H_1^{(1)}(x_0)][J_1(x_0) - \mathcal{T}_{-1}H_1^{(1)}(x_0)]}, \tag{18c}$$

with

$$\begin{aligned} \Pi_1 &= H_1^{(1)}(x_0)H_1^{(1)'}(x_0), & \Pi_2 &= H_1^{(1)'}(x_0)J_1(x_0), \\ \Pi_3 &= H_1^{(1)}(x_0)J_1'(x_0), & \Pi_4 &= J_1(x_0)J_1'(x_0). \end{aligned}$$

Then, from the magnetic permeability in Equation (1) the corresponding effective elements  $\mu_{re}$  and  $\mu_{ke}$  can be obtained from  $\mu'_{re}$  and  $\mu'_{ke}$ . It is noted that for the convenience of analysis the isotropic magnetic permeability is defined according to its gyromagnetic form [112]

$$\mu_{eff} = \frac{\mu_{re}^2 - \mu_{ke}^2}{\mu_{re}} = \frac{1}{\mu'_{re}}. \tag{19}$$

Besides the retrieval of effective constitutive parameters, the effective-medium theory can also be used to design the composite resonating building blocks with exotic properties, facilitating the design of metamaterials and metasurfaces.

### 3. Nonreciprocal Perfect Absorption by Composite MMs

To begin with, we construct the MMs with an array of ferrite rods arranged periodically in the air as a square lattice with lattice separation  $a = 9$  mm, where both pure ferrite rod (type I) and the hollow ferrite rod (type II) are considered for the convenience of comparison. The 5-layer MM slabs with each layer 201 ferrite rods are concerned, where the middle ferrite rod at the top layer is fixed at the origin and the surface normal is along the  $y$  axis. The Gaussian beam of TM polarization is incident downward from either left hand side or right hand side with the beam focus positioned at the origin. To examine the nonreciprocal properties of electromagnetic waves scattered at the interface of MM slabs, the reflectance ( $\mathcal{R}$ ), transmittance ( $\mathcal{T}$ ), and absorptance ( $\mathcal{A}$ ) are calculated with the variation of incident angle  $\theta_{inc}$  and damping factor  $\alpha$  based on the multiple scattering theory [115,116]. With the knowledge that the nonreciprocal properties are reinforced near the MSP resonance with its characteristic frequency determined by [111,112]

$$f_m = \frac{1}{2\pi} \left( \omega_0 + \frac{1}{2}\omega_m \right) = \gamma H_0 + \frac{1}{2}\gamma M_s. \tag{20}$$

For the BMF  $H_0 = 600$  Oe and the saturation magnetization  $M_s = 1750$  G, the MSP resonance frequency  $f_m = 4.1$  GHz, in the vicinity of which the working frequency is chosen as  $f = 4$  GHz. The results are shown in Figure 2, where the transmittance in panels (b) and (e) indicates that no electromagnetic waves can propagate through the MM slab, corresponding to the photonic band gap arising from the MSP resonance. Then, by examining the reflectance and absorptance it can be found that the evident asymmetry can be demonstrated with respect to the positive and negative incident angles, especially, for the large incident angles, which is the identification of nonreciprocal reflection and absorption.

In addition, by comparing the results from the MM slabs of type I and type II we can find that the MM made up of hollow ferrite rods exhibits better performance regarding



the nonreciprocal properties. Interestingly, hollow ferrite rod correspond to less absorbing material, but it induces even stronger absorption as indicated by the absorptance in panels (c) and (f). In particular, at the incident angle  $\theta_{inc} = -55^\circ$ , nearly 100% absorption is achieved for the MM slab of type I with the damping factor around  $4 \times 10^{-2}$ , suggesting the implementation of perfect absorption. Differently, at the incident angle  $\theta_{inc} = 55^\circ$  about 50% electromagnetic wave is reflected. The phenomenon is termed nonreciprocal perfect absorption, yet the small reflection at  $\theta_{inc} = 55^\circ$  corresponds to the poor performance. The ideal performance of nonreciprocal perfect absorption implies the perfect absorption at one incident angle, but at the symmetric incident angle a total reflection is achieved. Although this cannot happen due to the existence of the material loss, the reflection can be improved by minimizing the material loss and, simultaneously, guaranteeing the perfect absorption at the symmetric direction. The MM of type II is a kind choice, a close examination of the absorptance in Figure 2f shows that a much smaller damping factor is required to achieve the perfect absorption with  $\alpha \sim 10^{-3}$ . In this case, the reflectance is larger than 70%, a much better performance is obtained. By incorporating a dielectric core is a feasible methodology to further improve the nonreciprocal absorption, which is to be presented in the following part by optimizing the relevant parameters.

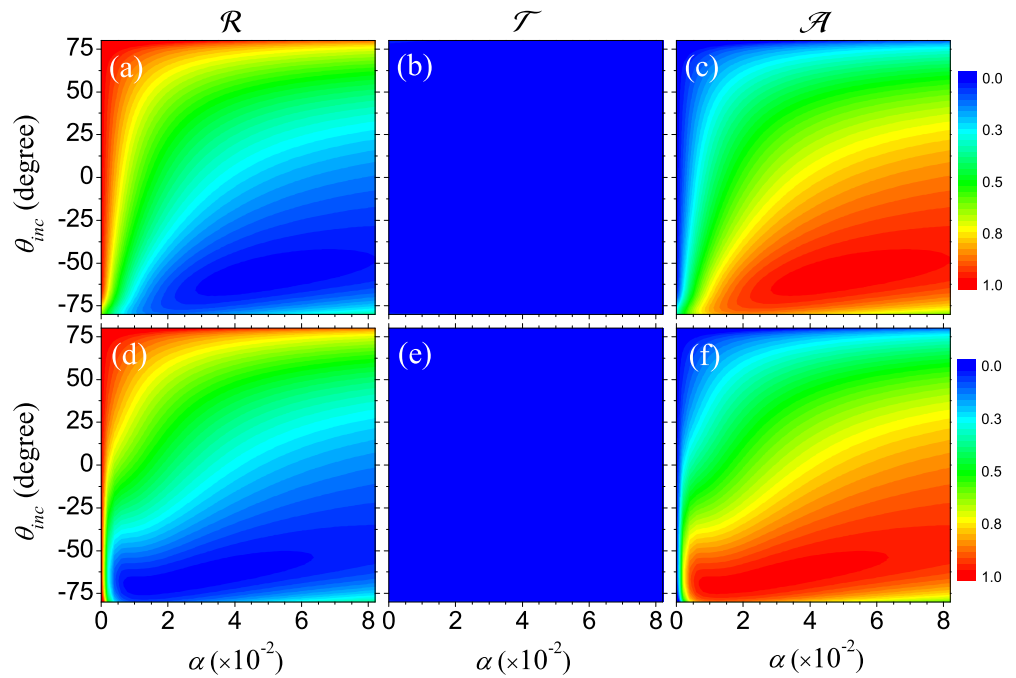


**Figure 2.** The reflectance (a,d), transmittance (b,e), and absorptance (c,f) are plotted as the functions of incident angle  $\theta_{inc}$  and damping factor  $\alpha$  for the 5-layer MM slabs made up of pure ferrite rods (a–c) and hollow ferrite rods (d–f), respectively. The MM slabs of type I and type II have the same lattice separation  $a = 9$  mm, two kinds of ferrite rods have the same outer radius  $r_s = 2.25$  mm, and the core radius of hollow ferrite rod is  $r_c = 0.8$  mm. The BMH is  $H_0 = 600$  Oe and the working frequency is  $f = 4$  GHz, locating at the vicinity of MSP resonance.

To describe nonreciprocal reflection and absorption quantitatively, we re-plot  $\mathcal{R}$ ,  $\mathcal{T}$ , and  $\mathcal{A}$  in Figure 2 with the specified parameters in Figure 3, where the nearly perfect nonreciprocal absorption with much smaller damping factor  $\alpha$  for the MM of type II can be found by comparing panels (a) and (d). From the spectra in Figure 3b,e, it can be found that the nonreciprocal perfect absorption can be solely achieved at a specified incident angle  $\theta_{inc}^c$  with the value dependent on the damping factor and the type of MM. The evident asymmetry of spectra with respect to the normal incidence ( $\theta_{inc} = 0^\circ$ ) clearly identifies the nonreciprocal reflection and absorption. To understand the phenomenon, the effective constitutive parameters are calculated based on the generalized effective-medium theory

as shown in Figure 3c,f, where the real part of effective permeability  $\mu_{eff}$  is negative, indicating the emergence of magnetic resonance. The single negative feature of effective parameters is responsible for the formation of photonic band gap and total reflection of electromagnetic waves. In addition, for both types of MMs the imaginary parts of  $\mu_{eff}$  are much larger than those of  $\varepsilon_{eff}$ , showing the dominant contribution of magnetic response to the nonreciprocal perfect absorption. Besides, the imaginary part of  $\mu_{eff}$  for the MM of type I is relatively larger than that of type II, which results in the weaker reflectance ( $\mathcal{R} = 55\%$ ) for the MM slab of type I than the reflectance ( $\mathcal{R} = 73\%$ ) for the MM slab of type II, thus degrading the nonreciprocal effect due to the larger damping factor.

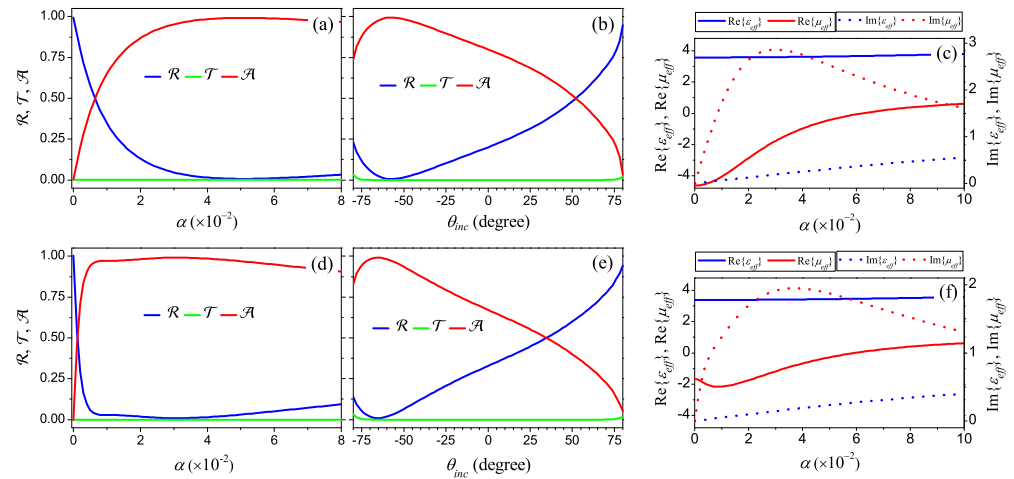


**Figure 3.**  $\mathcal{R}$ ,  $\mathcal{T}$ , and  $\mathcal{A}$  are plotted as the functions of damping factor  $\alpha$  (a), (d) at a fixed incident angle  $\theta_{inc} = 55^\circ$  and also plotted as the functions of the incident angle  $\theta_{inc}$  (b), (e) with a fixed damping factor  $5 \times 10^{-2}$  for the MM slab of type I (a,b) and type II (d,e). The effective permittivity  $\varepsilon_{eff}$  and effective permeability  $\mu_{eff}$  are plotted as the functions of the damping factor  $\alpha$  for the MM slab of type I (c) and type II (f). The bias magnetic field is  $H_0 = 600$  Oe and the working frequency is  $f = 4$  GHz and the other parameters are the same as those in Figure 2.

#### 4. Improving Nonreciprocity by Optimizing the DCL Ferrite Rod

From the aforementioned discussion, it is evident that the introduction of DCL ferrite rod is feasible to improve nonreciprocal performance. As the most simple case, the air core, namely, the hollow ferrite rod is considered at the first step of optimization to examine the possible limit we can achieve. Two critical parameters should be determined, i.e., the radius of air core  $r_c$  and the necessary damping factor  $\alpha$ , which can be acquired by calculating the spectra of  $\mathcal{R}$ ,  $\mathcal{T}$ , and  $\mathcal{A}$  as the functions of the core radius  $r_c$  and the damping factor  $\alpha$ . The results are shown in Figure 4, where the nonreciprocal absorption is realized with a very small damping factor  $\alpha = 5 \times 10^{-3}$  for the optimized air core radius  $r_c = 0.88$  mm as indicated by the dashed line in the reflectance and absorptance. This damping factor is one order of magnitude smaller than that for the MM slab of type I, which can remarkably minimize the absorption at the opposite incident angle  $\theta_{inc} = 55^\circ$ . The transmittance in Figure 4b shows that with the increase of the air core radius  $r_c$  the photonic band gap tends to vanish with  $r_c > 1.75$  mm and as is certain  $\mathcal{T} = 1$  for  $r_c = r_s$ , corresponding to the disappearance of MM slab. To demonstrate the optimized results quantitatively, the  $\mathcal{R}$ ,  $\mathcal{T}$ , and  $\mathcal{A}$  are re-plotted as the functions of damping factor  $\alpha$  at the fixed incident angle  $\theta_{inc} = -55^\circ$  as shown in Figure 4d, where the peak of absorptance or the dip of the reflectance indicates the optimized damping factor. In Figure 4e, the  $\mathcal{R}$ ,  $\mathcal{T}$ , and  $\mathcal{A}$  are plotted as the functions of incident angle  $\theta_{inc}$  with the optimized air core radius  $r_c = 0.88$  mm and the optimized damping factor  $\alpha = 5 \times 10^{-3}$ , where perfect absorption is achieved at the incident angle  $\theta_{inc} = -55^\circ$  and at the opposite incident angle  $\theta_{inc} = 55^\circ$  the reflectance is improved to be  $\mathcal{R} = 87.5\%$ , giving rise to a better performance of nonreciprocity. To explain the reason why such a small damping factor results in the nonre-

ciprocal perfect absorption, the effective constitutive parameters are calculated as shown in Figure 4f, where a prominent peak comes into appearance for  $\text{Im}\{\mu_{eff}\}$  with the amplitude comparable to that shown in Figure 3. This actually corresponds to a resonance as to be shown later on.

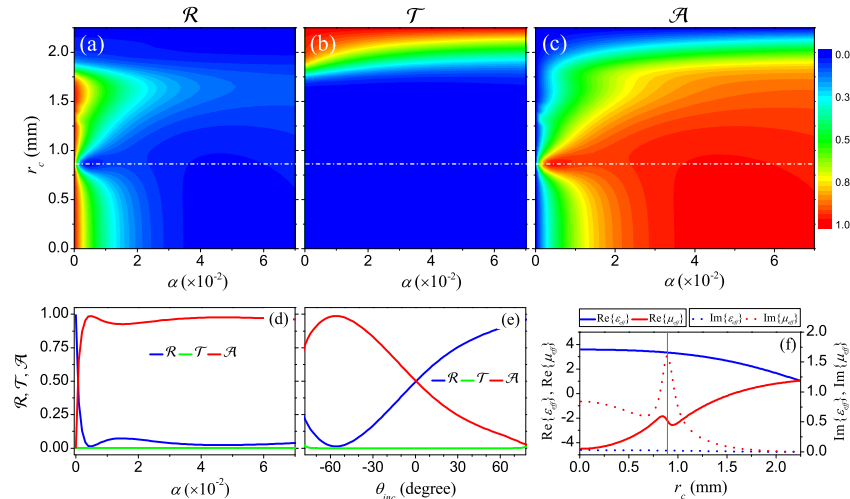


**Figure 4.**  $\mathcal{R}$  (a),  $\mathcal{T}$  (b), and  $\mathcal{A}$  (c) are plotted as the functions of damping factor  $\alpha$  and the inner radius  $r_c$  of hollow core for the MM slab of type II at a fixed incident angle  $\theta_{inc} = -55^\circ$ . The spectra are plotted as the functions of the damping factor  $\alpha$  (d) and the incident angle  $\theta_{inc}$  (e) for the optimized core radius  $r_c = 0.88$  mm. (f) The effective permittivity  $\epsilon_{eff}$  and effective permeability  $\mu_{eff}$  are plotted as the functions of core radius  $r_c$  at a fixed damping factor  $\alpha = 5 \times 10^{-3}$ . The BMF is  $H_0 = 600$  Oe, the working frequency is  $f = 4$  GHz and the other parameters are the same as those in Figure 2.

For the dielectric core with other permittivity, the MM of type III are constructed and the similar results are obtained and shown in Figure 5 for  $\epsilon_c = 15$ , where the optimized core radius is a little bit different as marked by the white dashed line in panels (a)–(c). As indicated by the  $\mathcal{R}$ ,  $\mathcal{T}$ , and  $\mathcal{A}$  spectra in Figure 5d, an even smaller damping factor  $\alpha = 3.5 \times 10^{-3}$  is adequate to achieve the nonreciprocal perfect absorption. By plotting the  $\mathcal{R}$ ,  $\mathcal{T}$ , and  $\mathcal{A}$  as the functions of the incident angle  $\theta_{inc}$  for the fixed damping factor  $\alpha = 3.5 \times 10^{-3}$ , it can be found that the perfect absorption is realized at the incident angle  $\theta_{inc} = -55^\circ$  and the reflection at the incident angle  $\theta_{inc} = 55^\circ$  is amount to  $\mathcal{R} = 89.5\%$ , improved a little bit compared to that in Figure 4. This can be explained by examining the effective parameters in Figure 5f, where the imaginary part of effective permeability  $\text{Im}\{\mu_{eff}\}$  at the peak is relatively larger than that in Figure 4f although the damping factor is relatively smaller. Regarding the dielectric core with other permittivity, the comparable nonreciprocal absorption can be found by optimizing the size of dielectric core, showing the same mechanism dominating the enhanced nonreciprocity. As shown in Figures 4 and 5, by optimizing the core radius  $r_c$  the enhanced nonreciprocal absorption can be acquired. Actually, the outer radius  $r_s$  of DCL ferrite rod can be served as another parameter to further improve the performance if the optimization of dielectric core cannot guarantee adequate quality.

To present a clear picture of nonreciprocal perfect absorption, the electric field patterns are simulated for a Gaussian beam of TM polarization striking on the MM slab of type II at the incident angles  $\theta_{inc} = \pm 55^\circ$  with mirror symmetry have been simulated based on the multiple scattering theory. The results are shown in Figure 6, where the specular reflection happens at the interface of lossless MM slab with damping factor  $\alpha = 0$  due to existence photonic band gap. As a result, not any nonreciprocal phenomenon can be observed by comparing the panels (a) and (d) although the scattering features of each DCL ferrite rod are different as to be shown in the following paragraph. The introduction of material loss can induce the absorption of electromagnetic waves due to the excitation of local modes of the DCL ferrite rods illuminated by the Gaussian beam. Therefore, the reflectance and

absorptance are dependent on the excited local modes, which causes the nonreciprocal effects due to the different incident angles as shown in panels (b) and (e). Regarding the Gaussian beam incident from right hand side with  $\theta_{inc} = 55^\circ$ , nearly 90 percent of the energy flow are reflected, while the electromagnetic wave is completely absorbed for the left hand side incidence with  $\theta_{inc} = -55^\circ$  due to the destructive interference of the excited modes, forming a sharp contrast to the constructive interference in panel (d). In addition, by reversing the magnetization to  $-z$  direction the nonreciprocal effect is reversed as shown in Figure 6c,f owing to the dependence of nonreciprocity on the BMF.

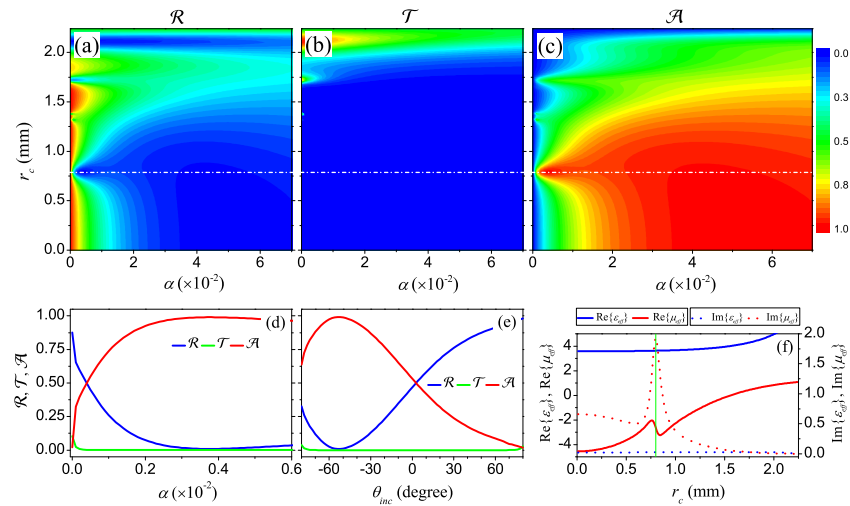


**Figure 5.**  $\mathcal{R}$  (a),  $\mathcal{T}$  (b), and  $\mathcal{A}$  (c) are plotted as the functions of damping factor  $\alpha$  and the inner radius  $r_c$  of dielectric core for the MM slab of type III at a fixed incident angle  $\theta_{inc} = -55^\circ$ . The spectra are plotted as the functions of the damping factor  $\alpha$  (d) and the incident angle  $\theta_{inc}$  (e) for the optimized core radius  $r_c = 0.8$  mm. (f) The effective permittivity  $\epsilon_{eff}$  and effective permeability  $\mu_{eff}$  are plotted as the functions of core radius  $r_c$  at a fixed damping factor  $\alpha = 3.5 \times 10^{-3}$ . The BMF is  $H_0 = 600$  Oe, the permittivity of dielectric core  $\epsilon_c = 15$  for DCL ferrite rod, the working frequency is  $f = 4$  GHz and the other parameters are the same as those in Figure 2.

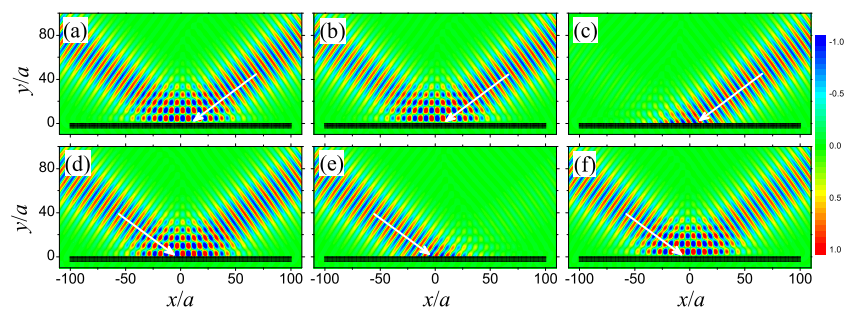


**Figure 6.** The electric field patterns illustrating the nonreciprocal perfect absorption for a Gaussian beam striking the composite MM slab of type II from the right hand side with  $\theta_{inc} = 55^\circ$  (a–c) and from the left hand side with  $\theta_{inc} = -55^\circ$  (d–f). The lossless MM slab with damping factors  $\alpha = 0$  (a,d), the lossy MM slab with damping factor  $\alpha = 5 \times 10^{-3}$  (b,e), and the lossy MM slab with damping factor  $\alpha = 5 \times 10^{-3}$  under reversed magnetization (c,f) are considered. The radius of dielectric core is  $r_c = 0.88$  mm, the BMF is  $H_0 = 600$  Oe, the working frequency is  $f = 4$  GHz, and the other parameters are the same as those in Figure 2.

To interpret the nonreciprocal perfect absorption and the enhancement of the nonreciprocity by the composite MMs of type II and III, the excited local modes of the ferrite rod positioned at the origin of MM slab have been simulated as shown in Figure 7, where a remarkable difference can be observed for the Gaussian beam incident from right (left)

hand side with the incident angle  $\theta_{inc} = 55^\circ$  ( $\theta_{inc} = -55^\circ$ ) as indicated by comparing the field patterns at odd and even columns. It is evident that the Gaussian beam incident from left hand side with  $\theta_{inc} = -55^\circ$  can effectively excite the eigenmodes, corresponding to the much stronger local fields, leading to the perfect absorption. Differently, the excited local fields by the incident Gaussian beam from right hand side is much weaker so that the absorptance is much smaller, corresponding to the reflection of Gaussian beam, thus explaining the nonreciprocal absorption effect. For the MM slab of type I as shown in columns (a) and (b), it can be found that the partial wave field is mainly associated with the angular momentum channel  $n = +1$ , which is responsible for the nonreciprocal absorption. As a comparison, for the MM slabs of type II and III the excited local field of DCL ferrite rod comes not only from the +1st order partial wave but also from the that of the  $-1$ st order as shown in columns (d), (f), and (h). In addition, the  $-1$ st order modes exist inside the DCL ferrite rod, which results in the much more effective absorption, thus explaining the substantial enhancement of nonreciprocity for the MMs of type II and III. Actually, the optimization procedure in Figures 4 and 5 is to find out the appropriate permittivity and radius of dielectric core so that the  $-1$ st order mode exist inside the DCL ferrite rod and can be excited nonreciprocally at specified direction.

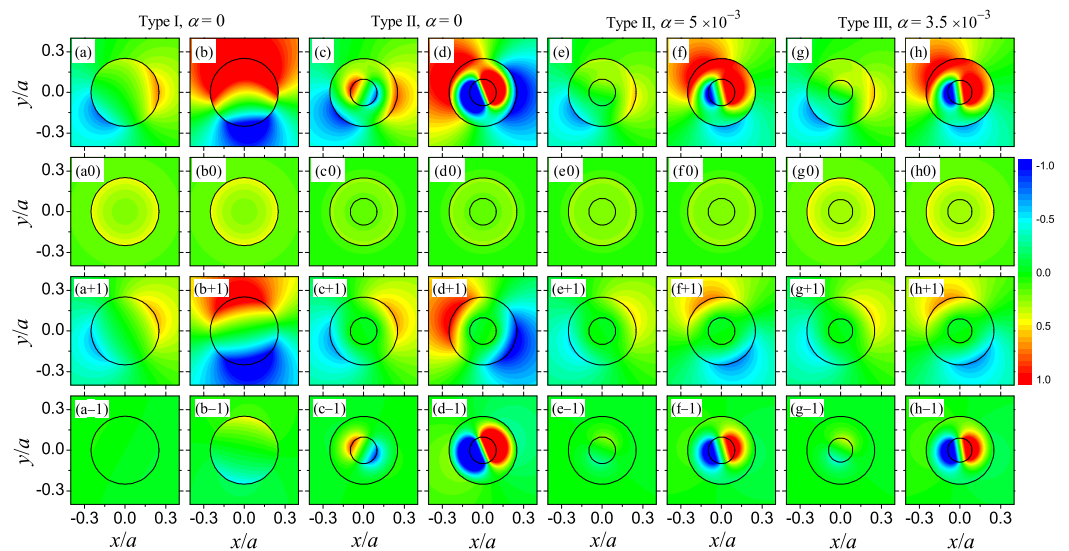


**Figure 7.** The scattered electric field from the ferrite rod positioned at the origin of MM slab of type I (a,b), type II (c,d) with damping factor  $\alpha = 0$  and  $\alpha = 5 \times 10^{-3}$  (e,f), and type III with damping factor  $\alpha = 3.5 \times 10^{-3}$  (g,h). The total scattered fields (the 1st row) and the scattered partial fields associated with the angular momentum channel of 0-th order (the 2nd row), +1st order (the 3rd row), and  $-1$ st order (the 4th row) are plotted for the incident angle  $\theta_{inc} = \pm 55^\circ$ . The permittivities are 1 and 15, the core radii are 0.88 mm and 0.8 mm for the MMs of type II and III, and the other parameters are the same as those in Figure 2.

### 5. Tunability by a BMF

Due to the direct dependence of MSP resonance on BMF as given in Equation (20), the nonreciprocal absorption effect should be flexibly tuned, which can be investigated by calculating the absorptance  $\mathcal{A}$  as the functions of BMF  $H_0$  and three other typical parameters, i.e., frequency  $f$ , incident angle  $\theta_{inc}$ , and damping factor  $\alpha$ . The results are shown in Figure 8, the operating frequency is shown to be tuned nearly in a linear manner as indicated by the white dashed line in panel (a), which can be further corroborated by re-plotting  $\mathcal{A}$  under three different BMFs  $H_0 = 530$  Oe, 600 Oe, and 670 Oe as shown in Figure 8d. The peak of red solid line is  $f = 4$  GHz, corresponding to the operating frequency under the BMF  $H_0 = 600$  Oe considered in previous sections. The other two peaks in green and blue solid lines correspond to the operating frequencies under two other BMFs, in good agreement with the linear relation between the MSP resonance frequency

and the BMF in Equation (20). The angular dependence of nonreciprocal absorption effect is also examined in Figure 8b, where the nonreciprocal absorption effect becomes weaker and weaker when the operating frequency  $f = 4$  GHz is far away from the MSP resonance frequency with the BMF deviated from 600 Oe, especially, from the nearly symmetric spectrum around 400 Oe as shown in Figure 8b. By plotting the absorptance  $\mathcal{A}$  under two different BMFs  $H_0 = 600$  Oe and 580 Oe, the angular dependence is demonstrated only in the range of large incident angle, in particular, the nearly perfect absorption with  $\mathcal{A} = 95\%$  is achieved at the incident angle  $\theta_{inc} = -80^\circ$  and at the opposite incident angle  $\theta_{inc} = 80^\circ$  a nearly total reflection with  $\mathcal{R} = 98\%$  is achieved under the BMF  $H_0 = 580$  Oe as shown in Figure 8e. By calculating the absorptance as the function of BMF  $H_0$  and damping factor  $\alpha$  as shown in Figure 8c, the minimal damping factor extracted in Figure 5 can still be the optimized one under the BMF  $H_0 = 600$  Oe. In addition, a very interesting issue is that a very small area close to this extremum with even smaller damping factor  $\alpha$  is discerned as marked by the black circle, which can be more discernable in panel (f), especially, in the inset (g), where the perfect absorption is achieved with the damping factor  $\alpha = 5 \times 10^{-4}$ . However, the MM of type III with this extraordinary damping factor does not exhibit evident nonreciprocal absorption, but possesses wide-angle absorption.

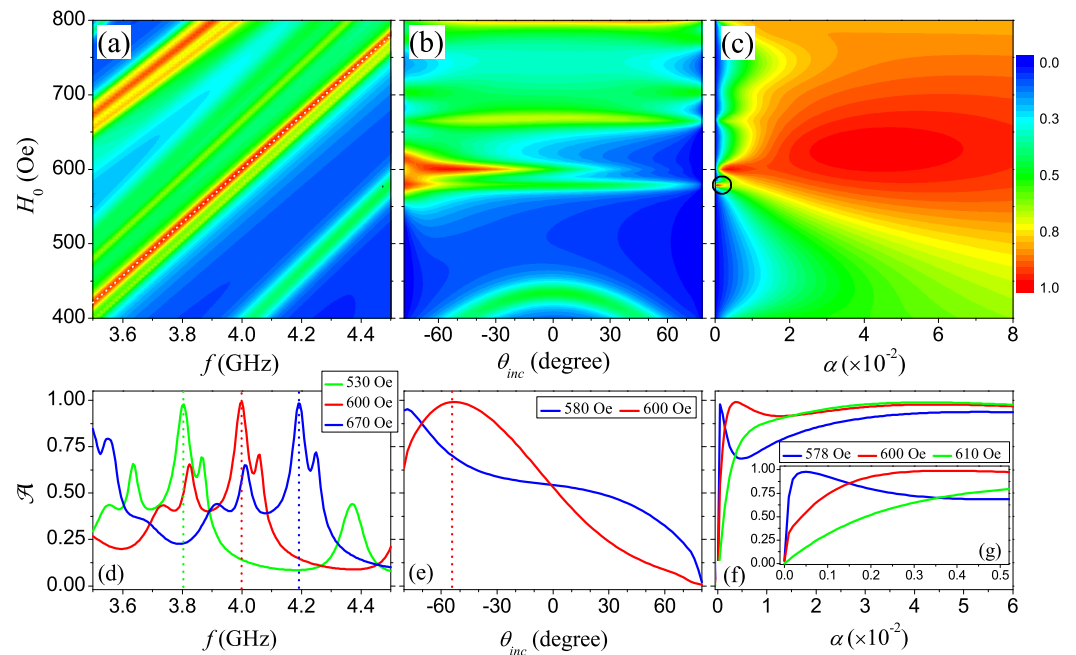


**Figure 8.** The tunability of nonreciprocal perfect absorption for the MM slab of type III by a BMF, shown by calculating the absorptance  $\mathcal{A}$  as the function of BMF  $H_0$  and working frequency  $f$  (a) at the specified incident angle  $\theta_{inc} = -55^\circ$  and fixed damping factor  $\alpha = 3.5 \times 10^{-3}$ , as the function of BMF  $H_0$  and incident angle  $\theta_{inc}$  (b) for the fixed damping factor  $\alpha = 3.5 \times 10^{-3}$  and working frequency  $f = 4$  GHz, as the function of BMF  $H_0$  and damping factor  $\alpha$  (c) for the fixed incident angle  $\theta_{inc} = -55^\circ$  and working frequency  $f = 4$  GHz. To quantitatively illustrate the dependence on BMF, (d) the absorptance  $\mathcal{A}$  in panel (a) under three different BMFs is re-plotted, (e) the absorptance  $\mathcal{A}$  in panel (b) under two different BMFs is re-plotted, and (f) the absorptance  $\mathcal{A}$  in panel (c) under three different BMFs is re-plotted. The inset (g) in panel (f) is the amplified view of the absorptance in the range of low damping factor. The permittivity of the DC in DCL ferrite rod is  $\epsilon_c = 15$ , the core radius is  $r_c = 0.8$  mm, and the other parameters are the same as those in Figure 2.

### 6. Conclusions

In summary, we have constructed composite MMs composed of an array of DCL ferrite rods with either hollow or dielectric cores, which can be employed to implement the NPs in that the perfect absorption is observed for the Gaussian beam incident at a specified direction, while a nearly total reflection is incurred at the symmetric incident direction. It is

demonstrated that the material loss plays a crucial role for the nonreciprocal absorption effect, but a very strong loss will degrade the nonreciprocity of the system. Based on the generalized effective-medium theory, it is shown that at the working frequency the effective magnetic permeability is negative, corresponding to the frequency in the vicinity of MSP resonance. In particular, the peak of  $\text{Im}\{\mu_{\text{eff}}\}$  for the MMs of type II and III with a much smaller damping factor has the comparable amplitude as that of the MM of type I, which explains the enhancement of nonreciprocal absorption effect. The partial wave analysis indicates that an additional  $-1$ st order resonance emerges inside the DCL ferrite rod, which corresponds to the appearance of absorption peak for the MMs of type II and III. In addition, the operating frequency can be flexibly controlled by tuning the magnitude of BMF and the nonreciprocity can also be reversed by use of the opposite magnetization. The concept proposed in this research can be extended to the optical region with magneto-optical materials and find more promising applications.

**Author Contributions:** S.L. conceived the idea. Y.C. derived the effective-medium theory and performed the simulations. S.L. and Y.C. wrote and finalized the manuscript. Y.Z., L.Z. (Lingzhong Zhao), G.W., L.Z. (Lin Zhang), Q.B., Q.L. and J.Y. discussed and commented on results in the manuscript. All authors have read and agreed to the published version of the manuscript.

**Funding:** This research was funded by National Natural Science Foundation of China (11574275) and Zhejiang Provincial Natural Science Foundation of China (LR16A040001). QL was supported by Middle-aged and Young Teachers' Basic Ability Promotion Project of Guangxi Province (2022KY1604).

**Institutional Review Board Statement:** Not applicable.

**Informed Consent Statement:** Not applicable.

**Data Availability Statement:** The data presented in this paper are available on request from the corresponding author.

**Conflicts of Interest:** The authors declare no conflict of interest.

## References

1. Walther, K. Reflection factor of gradual-transition absorbers for electromagnetic and acoustic waves. *IRE Trans. Anten. Propag.* **1960**, *8*, 608–621. [\[CrossRef\]](#)
2. Naito, Y.; Suetake, K. Application of ferrite to electromagnetic wave absorber and its characteristics. *IEEE Trans. Microwave Theory Tech.* **1971**, *MTT-19*, 65–72. [\[CrossRef\]](#)
3. Aoto, T.; Yoshida, N.; Fukai, I. Transient analysis of the electromagnetic field for a wave absorber in three-dimensional space. *IEEE Trans. Electromagn. Compat.* **1987**, *EMC-29*, 18–23. [\[CrossRef\]](#)
4. Kim, K.Y.; Kim, W.S.; Hong, S.Y. A study on the behaviour of laminated electromagnetic wave absorber. *IEEE Trans. Magn.* **1993**, *29*, 2134–2138.
5. Kim, D.I.; Takahashi, M.; Anzai, H.; Jun, S.Y. Electromagnetic wave absorber with wide-band frequency characteristics using exponentially tapered ferrite. *IEEE Trans. Electromagn. Compat.* **1996**, *38*, 173–177.
6. Huang, Y.F.; Chattopadhyay, S.; Jen, Y.J.; Peng, C.Y.; Liu, T.A.; Hsu, Y.K.; Pan, C.L.; Lo, H.C.; Hsu, C.H.; Chang, Y.H.; et al. Improved broadband and quasiomnidirectional anti-reflection properties with biomimetic silicon nanostructures. *Nat. Nanotechnol.* **2007**, *2*, 770–774. [\[CrossRef\]](#)
7. Yang, Z.P.; Ci, L.J.; Bur, J.A.; Lin, S.Y.; Ajayan, P.M. Experimental observation of an extremely dark material made by a low-density nanotube array. *Nano Lett.* **2008**, *8*, 446–451. [\[CrossRef\]](#)
8. Kim, T.; Do, H.W.; Choi, K.J.; Kim, S.; Lee, M.; Kim, T.; Yu, B.K.; Cheon, J.; Min, B.W.; Shim, W. Layered aluminum for electromagnetic wave absorber with near-zero reflection. *Nano Lett.* **2021**, *21*, 1132–1140. [\[CrossRef\]](#)
9. Liang, J.; Ye, F.; Cao, Y.C.; Mo, R.; Cheng, L.F.; Song, Q. Defect-engineered graphene/Si<sub>3</sub>N<sub>4</sub> multilayer alternating core-shell nanowire membrane: A plainified hybrid for broadband electromagnetic wave absorption. *Adv. Funct. Mater.* **2022**, *32*, 2200141. [\[CrossRef\]](#)
10. Hu, H.B.; Gao, J.H.; Wang, W.; Tang, S.W.; Zhou, L.; He, Q.; Wu, H.C.; Zheng, X.Y.; Li, X.Y.; Li, X.H.; et al. Ultra-broadband perfect absorber based on self-organizing multi-scale plasmonic nanostructures. *Appl. Mater. Today* **2022**, *26*, 101266. [\[CrossRef\]](#)
11. Cheng, J.Y.; Zhang, H.B.; Wang, H.H.; Huang, Z.H.; Raza, H.; Hou, C.X.; Zheng, G.P.; Zhang, D.Q.; Zheng, Q.B.; Che, R.C. Tailoring self-polarization of bimetallic organic frameworks with multiple polar units toward high-performance consecutive multi-band electromagnetic wave absorption at gigahertz. *Adv. Funct. Mater.* **2022**, *32*, 2201129. [\[CrossRef\]](#)
12. Wu, Z.C.; Cheng, H.W.; Jin, C.; Yang, B.T.; Xu, C.Y.; Pei, K.; Zhang, H.B.; Yang, Z.Q.; Che, R.C. Dimensional design and core-shell engineering of nanomaterials for electromagnetic wave absorption. *Adv. Mater.* **2022**, *34*, 2107538. [\[CrossRef\]](#)

13. Tao, H.; Li, N.I.; Bingham, C.M.; Zhang, X.; Averitt, R.D.; Padilla, W.J. A metamaterial absorber for the terahertz regime: Design, fabrication and characterization. *Opt. Express* **2008**, *16*, 7181–7188. [[CrossRef](#)]
14. Landy, N.I.; Sajuyigbe, S.; Mock, J.J.; Smith, D.R.; Padilla, W.J. Perfect metamaterial absorber. *Phys. Rev. Lett.* **2008**, *100*, 207402. [[CrossRef](#)]
15. Ma, Y.; Chen, Q.; Grant, J.; Saha, S.C.; Khalid, A.; Cumming, D.R. A terahertz polarization insensitive dual band metamaterial absorber. *Opt. Lett.* **2011**, *36*, 945–947. [[CrossRef](#)]
16. Liu, X.M.; Lan, C.W.; Bi, K.; Li, B.; Zhao, Q.; Zhou, J. Dual band metamaterial perfect absorber based on Mie resonances. *Appl. Phys. Lett.* **2016**, *109*, 062902. [[CrossRef](#)]
17. Yin, W.; Shen, Z.L.; Li, S.N.; Zhang, L.Y.; Chen, X.F. A three-dimensional dual-band terahertz perfect absorber as a highly sensitive sensor. *Front. Phys.* **2021**, *9*, 665280. [[CrossRef](#)]
18. Zhu, J.; Yin, J.G.; Wu, C.S. Tunable perfect absorber of graphene metamaterial in the terahertz band and its sensing properties. *Adv. Photonics Res.* **2022**, *3*, 2100291. [[CrossRef](#)]
19. Shen, X.P.; Yang, Y.; Zang, Y.Z.; Gu, J.Q.; Han, J.G.; Zhang, W.L.; Cui, T.J. Triple-band terahertz metamaterial absorber: Design, experiment, and physical interpretation. *Appl. Phys. Lett.* **2012**, *101*, 154102. [[CrossRef](#)]
20. Wang, G.Z.; Wang, B.X. Five-band terahertz metamaterial absorber based on a four-gap comb resonator. *J. Light. Technol.* **2015**, *33*, 5151–5156. [[CrossRef](#)]
21. Bao, Z.Y.; Wang, J.C.; Hu, Z.D.; Balmakou, A.; Khakhomov, S.; Tang, Y.; Zhang, C.L. Coordinated multi-band angle insensitive selection absorber based on graphene metamaterials. *Opt. Express* **2019**, *27*, 31435–31445. [[CrossRef](#)]
22. Hu, D.; Wang, H.Y.; Zhu, Q.F. Design of six-band terahertz perfect absorber using a simple u-shaped closed-ring resonator. *IEEE Photon. J.* **2016**, *8*, 5500608. [[CrossRef](#)]
23. Wang, J.Q.; Fan, C.Z.; Ding, P.; He, J.N.; Cheng, Y.G.; Hu, W.Q.; Cai, G.W.; Liang, E.J.; Xue, Q.Z. Tunable broad-band perfect absorber by exciting of multiple plasmon resonances at optical frequency. *Opt. Express* **2012**, *20*, 14871–14878. [[CrossRef](#)]
24. Kenney, M.; Grant, J.; Shah, Y.D.; Escorcía-Carranza, I.; Humphreys, M.; Cumming, D.R.S. Octave-spanning broadband absorption of terahertz light using metasurface fractal-cross absorbers. *ACS Photon.* **2017**, *4*, 2604–2612. [[CrossRef](#)]
25. Huang, Y.J.; Liu, L.; Pu, M.B.; Li, X.; Ma, X.L.; Luo, X.G. A refractory metamaterial absorber for ultra-broadband, omnidirectional and polarization-independent absorption in the UV-NIR spectrum. *Nanoscale* **2018**, *10*, 8298–8303. [[CrossRef](#)]
26. Huang, Y.W.; Kaj, K.; Chen, C.X.; Yang, Z.W.; Haque, S.R.U.; Zhang, Y.; Zhao, X.G.; Averitt, R.D.; Zhang, X. Broadband terahertz silicon membrane metasurface absorber. *ACS Photon.* **2022**, *9*, 1150–1156. [[CrossRef](#)]
27. Zhu, B.; Feng, Y.J.; Zhao, J.M.; Huang, C.; Jiang, T. Switchable metamaterial reflector/absorber for different polarized electromagnetic waves. *Appl. Phys. Lett.* **2010**, *97*, 051906. [[CrossRef](#)]
28. Meng, L.J.; Zhao, D.; Li, Q.; Qiu, M. Polarization-sensitive perfect absorbers at near-infrared wavelengths. *Opt. Express* **2013**, *21*, A111–A122. [[CrossRef](#)]
29. Wang, W.H.; Besteiro, L.V.; Liu, T.J.; Wu, C.; Sun, J.C.; Yu, P.; Chang, L.; Wang, Z.M.; Govorov, A.O. Generation of hot electrons with chiral metamaterial perfect absorbers: Giant optical chirality for polarization-sensitive photochemistry. *ACS Photon.* **2019**, *6*, 3241–3252. [[CrossRef](#)]
30. Wen, Y.; Liang, Z.K.; Lin, Y.S. Tunable perfect meta-absorber with high-sensitive polarization characteristic. *Adv. Photonics Res.* **2021**, *2*, 2000027. [[CrossRef](#)]
31. Feng, R.; Qiu, J.; Cao, Y.Y.; Liu, L.H.; Ding, W.Q.; Chen, L.X. Omnidirectional and polarization insensitive nearly perfect absorber in one dimensional meta-structure. *Appl. Phys. Lett.* **2014**, *105*, 181102. [[CrossRef](#)]
32. Tian, X.M.; Li, Z.Y. Visible-near infrared ultra-broadband polarization-independent metamaterial perfect absorber involving phase-change materials. *Photon. Res.* **2016**, *4*, 146–152. [[CrossRef](#)]
33. Kang, M.; Zhang, H.F.; Zhang, X.Q.; Yang, Q.L.; Zhang, W.L.; Han, J.G. Interferometric control of dual-band terahertz perfect absorption using a designed metasurface. *Phys. Rev. Appl.* **2018**, *9*, 054018. [[CrossRef](#)]
34. Li, H.J.; Wei, G.G.; Zhou, H.M.; Xiao, H.X.; Qin, M.; Xia, S.X.; Wu, F. Polarization-independent near-infrared superabsorption in transition metal dichalcogenide Huygens metasurfaces by degenerate critical coupling. *Phys. Rev. B* **2022**, *105*, 165305. [[CrossRef](#)]
35. Avitzour, Y.; Urzhumov, Y.A.; Shvets, G. Wide-angle infrared absorber based on a negative-index plasmonic metamaterial. *Phys. Rev. B* **2009**, *79*, 045131. [[CrossRef](#)]
36. Wu, C.H.; Neuner, B., III; Shvets, G. Large-area wide-angle spectrally selective plasmonic absorber. *Phys. Rev. B* **2011**, *84*, 075102. [[CrossRef](#)]
37. Wang, X.; Jiang, X.; You, Q.; Guo, J.; Dai, X.Y.; Xiang, Y.J. Tunable and multichannel terahertz perfect absorber due to Tamm surface plasmons with graphene. *Photon. Res.* **2017**, *5*, 536–542. [[CrossRef](#)]
38. Hou, W.J.; Yang, F.; Chen, Z.M.; Dong, J.W.; Jiang, S.J. Wide-angle and broadband solar absorber made using highly efficient large-area fabrication strategy. *Opt. Express* **2022**, *30*, 4424–4433. [[CrossRef](#)]
39. Teperik, T.V.; García De Abajo, F.J.; Borisov, A.G.; Abdelsalam, M.; Bartlett, P.N.; Sugawara, Y.; Baumberg, J.J. Omnidirectional absorption in nanostructured metal surfaces. *Nat. Photon.* **2008**, *2*, 299–301. [[CrossRef](#)]
40. Zhang, H.; Liu, F.J.; Blaikie, R.J.; Ding, B.Y.; Qiu, M. Bifacial omnidirectional and band-tunable light absorption in free-standing core-shell resonators. *Appl. Phys. Lett.* **2022**, *120*, 181110. [[CrossRef](#)]
41. Atwater, H.A.; Polman, A. Plasmonics for improved photovoltaic devices. *Nat. Mater.* **2010**, *9*, 205–213. [[CrossRef](#)]



42. Akselrod, G.M.; Huang, J.N.; Hoang, T.B.; Bowen, P.T.; Su, L.; Smith, D.R.; Mikkelsen, M.H. Large-area metasurface perfect absorbers from visible to near-infrared. *Adv. Mater.* **2015**, *27*, 8028–8034. [[CrossRef](#)]
43. Yu, W.W.; Lu, Y.; Chen, X.R.; Xu, H.; Shao, J.; Chen, X.; Sun, Y.; Hao, J.M.; Dai, N. Large-area, broadband, wide-angle plasmonic metasurface absorber for midwavelength infrared atmospheric transparency window. *Adv. Opt. Mater.* **2019**, *7*, 1900841. [[CrossRef](#)]
44. Li, W.; Valentine, J. Metamaterial perfect absorber based hot electron photodetection. *Nano Lett.* **2014**, *14*, 3510–3514. [[CrossRef](#)]
45. Zhan, Y.H.; Wu, K.; Zhang, C.; Wu, S.L.; Li, X.F. Infrared hot-carrier photodetection based on planar perfect absorber. *Opt. Lett.* **2015**, *40*, 4261–4264. [[CrossRef](#)]
46. Chen, Z.; Weng, Y.D.; Liu, J.K.; Guo, N.; Yu, Y.L.; Xiao, L. Dual-band perfect absorber for a mid-infrared photodetector based on a dielectric metal metasurface. *Photon. Res.* **2021**, *9*, 27–33. [[CrossRef](#)]
47. Fang, Y.R.; Jiao, Y.; Xiong, K.L.; Ogier, R.; Yang, Z.J.; Gao, S.W.; Dahlin, A.B.; Käll, M. Plasmon enhanced internal photoemission in antenna-spacer-mirror based Au/TiO<sub>2</sub> nanostructures. *Nano Lett.* **2015**, *15*, 4059–4065. [[CrossRef](#)]
48. Ng, C.; Cadusch, J.J.; Dligatch, S.; Roberts, A.; Davis, T.J.; Mulvaney, P.; Gómez, D.E. Hot carrier extraction with plasmonic broadband absorbers. *ACS Nano* **2016**, *10*, 4704–4711. [[CrossRef](#)]
49. Tan, F.R.; Wang, N.; Lei, D.Y.; Yu, W.X.; Zhang, X.M. Plasmonic black absorbers for enhanced photocurrent of visible-light photocatalysis. *Adv. Opt. Mater.* **2017**, *5*, 1600399. [[CrossRef](#)]
50. Maier, T.; Brueckl, H. Multispectral microbolometers for the midinfrared. *Opt. Lett.* **2010**, *35*, 3766–3768. [[CrossRef](#)]
51. Grant, J.; Escorcia-Carranza, I.; Li, C.; McCrindle, I.J.H.; Gough, J.; Cumming, D.R.S. A monolithic resonant terahertz sensor element comprising a metamaterial absorber and micro-bolometer. *Laser Photon. Rev.* **2013**, *7*, 1043–1048. [[CrossRef](#)]
52. Kong, X.T.; Khorashad, L.K.; Wang, Z.M.; Govorov, A.O. Photothermal circular dichroism induced by plasmon resonances in chiral metamaterial absorbers and bolometers. *Nano Lett.* **2018**, *18*, 2001–2008. [[CrossRef](#)] [[PubMed](#)]
53. Liu, N.; Mesch, M.; Weiss, T.; Hentschel, M.; Giessen, H. Infrared perfect absorber and its application as plasmonic sensor. *Nano Lett.* **2010**, *10*, 2342–2348. [[CrossRef](#)] [[PubMed](#)]
54. Ou, H.L.; Lu, F.Y.; Xu, Z.F.; Lin, Y.S. Terahertz metamaterial with multiple resonances for biosensing application. *Nanomaterials* **2020**, *10*, 1038. [[CrossRef](#)] [[PubMed](#)]
55. Seyyedmasoumian, S.; Attariabad, A.; Pourziad, A.; Bemani, M. Refractive index biosensor using metamaterial perfect absorber based on graphene in near-infrared for disease diagnosis. *IEEE Sens. J.* **2022**, *22*, 14870–14877. [[CrossRef](#)]
56. Chen, Q.; Hu, X.; Wen, L.; Yu, Y.; Cumming, D.R.S. Nanophotonic image sensors. *Small* **2016**, *12*, 4922–4935. [[CrossRef](#)] [[PubMed](#)]
57. Rakhshani, M.R. Three-dimensional polarization-insensitive perfect absorber using nanorods array for sensing and imaging. *IEEE Sens. J.* **2020**, *20*, 14166–14172. [[CrossRef](#)]
58. Sharma, A.; Kedia, J.; Gupta, N. Emerging nanostructured infrared absorbers enabling cost-effective image sensing: A review. *Opt. Eng.* **2021**, *60*, 090901.
59. Diem, M.; Koschny, T.; Soukoulis, C.M. Wide-angle perfect absorber/thermal emitter in the terahertz regime. *Phys. Rev. B* **2009**, *79*, 033101. [[CrossRef](#)]
60. Liu, X.L.; Tyler, T.; Starr, T.; Starr, A.F.; Jokerst, N.M.; Padilla, W.J. Taming the blackbody with infrared metamaterials as selective thermal emitters. *Phys. Rev. Lett.* **2011**, *107*, 045901. [[CrossRef](#)]
61. Du, K.K.; Li, Q.; Lyu, Y.B.; Ding, J.C.; Lu, Y.; Cheng, Z.Y.; Qiu, M. Control over emissivity of zero-static-power thermal emitters based on phase-changing material GST. *Light Sci. Appl.* **2017**, *6*, e16194. [[CrossRef](#)]
62. Watts, C.M.; Shrekenhamer, D.; Montoya, J.; Lipworth, G.; Hunt, J.; Sleasman, T.; Krishna, S.; Smith, D.R.; Padilla, W.J. Terahertz compressive imaging with metamaterial spatial light modulators. *Nat. Photon.* **2014**, *8*, 605–609. [[CrossRef](#)]
63. Carrillo, S.G.C.; Nash, G.R.; Hayat, H.; Cryan, M.J.; Klemm, M.; Bhaskaran, H.; Wright, C.D. Design of practicable phase-change metadevices for near-infrared absorber and modulator applications. *Opt. Express* **2016**, *24*, 13563–13573. [[CrossRef](#)]
64. Li, W.L.; Hu, X.M.; Wu, J.B.; Fan, K.B.; Chen, B.W.; Zhang, C.H.; Hu, W.; Cao, X.; Jin, B.B.; Lu, Y.Q.; et al. Dual-color terahertz spatial light modulator for single-pixel imaging. *Light Sci. Appl.* **2022**, *11*, 191. [[CrossRef](#)]
65. Wan, W.J.; Chong, Y.D.; Ge, L.; Noh, H.; Stone, A.D.; Cao, H. Time-reversed lasing and interferometric control of absorption. *Science* **2011**, *331*, 889–892. [[CrossRef](#)]
66. Fu, Y.Y.; Cao, Y.Y.; Cummer, S.A.; Xu, Y.D.; Chen, H.Y. Coherent perfect absorber and laser modes in purely imaginary metamaterials. *Phys. Rev. A* **2017**, *96*, 043838. [[CrossRef](#)]
67. Wang, C.; Shen, X.; Chu, H.C.; Luo, J.; Zhou, X.X.; Hou, B.; Peng, R.W.; Wang, M.; Lai, Y. Realization of broadband coherent perfect absorption of spoof surface plasmon polaritons. *Appl. Phys. Lett.* **2022**, *120*, 171703. [[CrossRef](#)]
68. Sun, Y.; Tan, W.; Li, H.Q.; Li, J.; Chen, H. Experimental demonstration of a coherent perfect absorber with PT phase transition. *Phys. Rev. Lett.* **2014**, *112*, 143903. [[CrossRef](#)]
69. Farhat, M.; Yang, M.Y.; Ye, Z.L.; Chen, P.Y. PT-symmetric absorber-laser enables electromagnetic sensors with unprecedented sensitivity. *ACS Photon.* **2020**, *7*, 2080–2088. [[CrossRef](#)]
70. Yu, J.B.; Ma, B.Z.; Ouyang, A.; Ghosh, P.; Luo, H.; Pattanayak, A.; Kaur, S.; Qiu, M.; Belov, P.; Li, Q. Dielectric super-absorbing metasurfaces via PT symmetry breaking. *Optica* **2021**, *8*, 1290–1295. [[CrossRef](#)]
71. Bai, P.; Ding, K.; Wang, G.; Luo, J.; Zhang, Z.Q.; Chan, C.T.; Wu, Y.; Lai, Y. Simultaneous realization of a coherent perfect absorber and laser by zero-index media with both gain and loss. *Phys. Rev. A* **2016**, *94*, 063841. [[CrossRef](#)]

72. Hendrickson, J.R.; Vangala, S.; Dass, C.; Gibson, R.; Goldsmith, J.; Leedy, K.; Walker, D.E., Jr.; Cleary, J.W.; Kim, W.; Guo, J.P. Coupling of epsilon-near-zero mode to gap plasmon mode for flat-top wideband perfect light absorption. *ACS Photon.* **2018**, *5*, 776–781. [[CrossRef](#)]
73. Castillo, M.A.; Estévez-Varela, C.; Wardley, W.P.; Serna, R.; Pastoriza-Santos, I.; Núñez-Sánchez, S.; Lopez-Garcia, M. Enhanced light absorption in all-polymer biomimetic photonic structures by near-zero-index organic matter. *Adv. Funct. Mater.* **2022**, *32*, 2113039. [[CrossRef](#)]
74. Johns, B.; Chattopadhyay, S.; Mitra, J. Tailoring infrared absorption and thermal emission with ultrathin film interferences in epsilon-near-zero media. *Adv. Photonics Res.* **2022**, *3*, 2100153. [[CrossRef](#)]
75. Genov, D.A.; Zhang, S.; Zhang, X. Mimicking celestial mechanics in metamaterials. *Nat. Phys.* **2009**, *5*, 687–692. [[CrossRef](#)]
76. Liu, S.Y.; Li, L.; Lin, Z.F.; Chen, H.Y.; Zi, J.; Chan, C.T. Graded index photonic hole: Analytical and rigorous full wave solution. *Phys. Rev. B* **2010**, *82*, 054204. [[CrossRef](#)]
77. Sheng, C.; Liu, H.; Wang, Y.; Zhu, S.N.; Genov, D.A. Trapping light by mimicking gravitational lensing. *Nat. Photon.* **2013**, *7*, 902–906. [[CrossRef](#)]
78. Wen, G.F.; Zhao, L.Z.; Zhang, L.; Chen, Y.Y.; Luo, Q.L.; Fang, A.A.; Liu, S.Y. Tunable beam propagation based on cylindrically symmetric gradient index system. *Acta Phys. Sin.* **2022**, *14*, 144201. [[CrossRef](#)]
79. Wang, X.; Duan, J.Y.; Chen, W.Y.; Zhou, C.B.; Liu, T.T.; Xiao, S.Y. Controlling light absorption of graphene at critical coupling through magnetic dipole quasi-bound states in the continuum resonance. *Phys. Rev. B* **2020**, *102*, 155432. [[CrossRef](#)]
80. Tian, J.Y.; Li, Q.; Belov, P.A.; Sinha, R.K.; Qian, W.P.; Qiu, M. High-Q all-dielectric metasurface: Super and suppressed optical absorption. *ACS Photon.* **2020**, *7*, 1436–1443. [[CrossRef](#)]
81. Saadabad, R.M.; Huang, L.J.; Miroshnichenko, A.E. Polarization-independent perfect absorber enabled by quasibound states in the continuum. *Phys. Rev. B* **2021**, *104*, 235405. [[CrossRef](#)]
82. Zhao, X.G.; Zhang, J.D.; Fan, K.B.; Duan, G.W.; Metcalfe, G.D.; Wraback, M.; Zhang, X.; Averitt, R.D. Nonlinear terahertz metamaterial perfect absorbers using GaAs. *Photon. Res.* **2016**, *4*, A16–A21. [[CrossRef](#)]
83. Nahvi, E.; Liberal, I.; Engheta, N. Nonlinear metamaterial absorbers enabled by photonic doping of epsilon-near-zero metastructures. *Phys. Rev. B* **2020**, *102*, 035404. [[CrossRef](#)]
84. Luo, Z.J.; Ren, X.Y.; Zhou, L.; Chen, Y.; Cheng, Q.; Ma, H.F.; Cui, T.J. A high-performance nonlinear metasurface for spatial-wave absorption. *Adv. Funct. Mater.* **2022**, *32*, 2109544. [[CrossRef](#)]
85. Mei, J.; Ma, G.C.; Yang, M.; Yang, Z.Y.; Wen, W.J.; Sheng, P. Dark acoustic metamaterials as super absorbers for low-frequency sound. *Nat. Commun.* **2012**, *3*, 756. [[CrossRef](#)]
86. Shao, C.; Zhu, Y.Z.; Long, H.Y.; Liu, C.; Cheng, Y.; Liu, X.J. Metasurface absorber for ultra-broadband sound via over-damped modes coupling. *Appl. Phys. Lett.* **2022**, *120*, 083504. [[CrossRef](#)]
87. Dong, H.W.; Zhao, S.D.; Oudich, M.; Shen, C.; Zhang, C.Z.; Cheng, L.; Wang, Y.S.; Fang, D.N. Reflective metasurfaces with multiple elastic mode conversions for broadband underwater sound absorption. *Phys. Rev. Appl.* **2022**, *17*, 044013. [[CrossRef](#)]
88. Qu, S. C.; Gao, N.; Tinel, A.; Morvan, B.; Romero-García, V.; Groby, J.P.; Sheng, P. Underwater metamaterial absorber with impedance-matched composite. *Sci. Adv.* **2022**, *8*, eabm4206. [[CrossRef](#)]
89. Shrekenhamer, D.; Chen, W.C.; Padilla, W.J. Liquid crystal tunable metamaterial absorber. *Phys. Rev. Lett.* **2013**, *110*, 177403. [[CrossRef](#)]
90. Isić, G.; Vasić, B.; Zografopoulos, D.C.; Beccherelli, R.; Gajić, R. Electrically tunable critically coupled terahertz metamaterial absorber based on nematic liquid crystals. *Phys. Rev. Appl.* **2015**, *3*, 064007. [[CrossRef](#)]
91. Lv, J.F.; Ding, C.; Meng, F.Y.; Han, J.Q.; Jin, T.; Wu, Q. A tunable metamaterial absorber based on liquid crystal with the compact unit cell and the wideband absorption. *Liq. Cryst.* **2021**, *48*, 1438–1447. [[CrossRef](#)]
92. Qi, L.M.; Liu, C.; Shah, S.M.A. A broad dual-band switchable graphene-based terahertz metamaterial absorber. *Carbon* **2019**, *153*, 179–188. [[CrossRef](#)]
93. Guo, Z.Y.; Yang, X.; Shen, F.; Zhou, Q.F.; Gao, J.; Guo, K. Active-tuning and polarization-independent absorber and sensor in the infrared region based on the phase change material of Ge<sub>2</sub>Sb<sub>2</sub>Te<sub>5</sub> (GST). *Sci. Rep.* **2018**, *8*, 12433. [[CrossRef](#)]
94. Lei, L.; Lou, F.; Tao, K.Y.; Huang, H.X.; Cheng, X.; Xu, P. Tunable and scalable broadband metamaterial absorber involving VO<sub>2</sub>-based phase transition. *Photon. Res.* **2019**, *7*, 734–741. [[CrossRef](#)]
95. Kang, Q.L.; Li, D.K.; Wang, W.; Guo, K.; Guo, Z.Y. Multiband tunable thermal camouflage compatible with laser camouflage based on GST plasmonic metamaterial. *J. Phys. D Appl. Phys.* **2022**, *55*, 065103. [[CrossRef](#)]
96. Liu, Y.N.; Weng, X.L.; Wang, M.R.; Li, W.X.; Ma, S.L.; Zhang, L.; Zhou, P.H.; Deng, L.J. Full control of Fano spectral profile with GST-based metamaterial. *ACS Photon.* **2022**, *9*, 888–894. [[CrossRef](#)]
97. Pitchappa, P.; Ho, C.P.; Kropelnicki, P.; Singh, N.; Kwong, D.L.; Lee, C. Micro-electro-mechanically switchable near infrared complementary metamaterial absorber. *Appl. Phys. Lett.* **2014**, *104*, 201114. [[CrossRef](#)]
98. Cong, L.Q.; Pitchappa, P.; Lee, C.K.; Singh, R. Active phase transition via loss engineering in a terahertz MEMS metamaterial. *Adv. Mater.* **2017**, *29*, 1700733. [[CrossRef](#)]
99. Piper, L.K.; Singh, H.J.; Woods, J.R.C.; Sun, K.; Muskens, O.L.; Apostolopoulos, V. Mechanically tunable terahertz metamaterial perfect absorber. *Adv. Photonics Res.* **2021**, *2*, 2100136. [[CrossRef](#)]
100. Liu, S.Y.; Chen, W.K.; Du, J.J.; Lin, Z.F.; Chui, S.T.; Chan, C.T. Manipulating negative-refractive behavior with a magnetic field. *Phys. Rev. Lett.* **2008**, *101*, 157407. [[CrossRef](#)]

101. Yu, X.N.; Chen, H.J.; Lin, H.X.; Zhou, J.L.; Yu, J.J.; Qian, C.X.; Liu, S.Y. Continuously tuning effective refractive index based on thermally controllable magnetic metamaterials. *Opt. Lett.* **2014**, *39*, 4643–4646. [[CrossRef](#)]
102. Luo, Q.L.; Zhao, L.Z.; Zhou, J.L.; Zhang, L.; Wen, G.F.; Ba, Q.T.; Wu, H.B.; Lin, Z.F.; Liu, S.Y. Magnetically reconfigurable unidirectional propagation of electromagnetic waves by zero-index-based heterostructured metamaterials. *Front. Mater.* **2022**, *9*, 845344. [[CrossRef](#)]
103. Liu, S.Y.; Lu, W.L.; Lin, Z.F.; Chui, S.T. Magnetically controllable unidirectional electromagnetic waveguiding devices designed with metamaterials. *Appl. Phys. Lett.* **2010**, *97*, 201113. [[CrossRef](#)]
104. Chui, S.T.; Liu, S.Y.; Lin, Z.F. Reflected wave of finite circulation from magnetic photonic crystals. *J. Phys. Condens. Matter* **2010**, *22*, 182201. [[CrossRef](#)]
105. Liu, S.Y.; Lu, W.L.; Lin, Z.F.; Chui, S.T. Molding reflection from metamaterials based on magnetic surface plasmons. *Phys. Rev. B* **2011**, *84*, 045425. [[CrossRef](#)]
106. Wang, M.D.; Zhang, R.Y.; Zhang, L.; Wang, D.Y.; Guo, Q.H.; Zhang, Z.Q.; Chan, C.T. Topological one-way large-area waveguide states in magnetic photonic crystals. *Phys. Rev. Lett.* **2021**, *126*, 067401. [[CrossRef](#)] [[PubMed](#)]
107. Zhao, L.Z.; Wen, G.F.; Zhang, L.; Tong, J.X.; You, Y.C.; Ba, Q.T.; Luo, Q.L.; Liu, S.Y. Reconfigurable unidirectional propagation of electromagnetic waves in photonic crystal waveguides. *J. Opt. Soc. Am. B* **2022**, *39*, 2443–2449. [[CrossRef](#)]
108. Wu, H.B.; Luo, Q.L.; Chen, H.J.; Han, Y.; Yu, X.N.; Liu, S.Y. Magnetically controllable nonreciprocal Goos-Hänchen shift supported by a magnetic plasmonic gradient metasurface. *Phys. Rev. A* **2019**, *99*, 033820. [[CrossRef](#)]
109. Chen, H.J.; Lu, W.L.; Li, J.J.; Yu, J.J.; Lin, Z.F.; Chan, C.T.; Liu, S.Y. Manipulating unidirectional edge states via magnetic plasmonic gradient metasurfaces. *Plasmonics* **2017**, *12*, 1079–1090. [[CrossRef](#)]
110. Wu, H.B.; Xi, X.; Li, X.M.; Poo, Y.; Liu, S.Y.; Wu, R.X. Manipulating electromagnetic radiation of one-way edge states by magnetic plasmonic gradient metasurfaces. *Photon. Res.* **2022**, *10*, 610–617. [[CrossRef](#)]
111. Liu, S.Y.; Du, J.J.; Lin, Z.F.; Wu, R.X.; Chui, S.T. Formation of robust and completely tunable resonant photonic band gaps. *Phys. Rev. B* **2008**, *78*, 155101. [[CrossRef](#)]
112. Pozar, D.M. *Microwave Engineering*, 4th ed.; John Wiley & Sons: New York, NY, USA, 2012; pp. 451–464.
113. Wu, Y.; Li, J.; Zhang, Z.Q.; Chan, C.T. Effective medium theory for magnetodielectric composites: Beyond the long-wavelength limit. *Phys. Rev. B* **2006**, *74*, 085111. [[CrossRef](#)]
114. Jin, J.F.; Liu, S.Y.; Lin, Z.F.; Chui, S.T. Effective-medium theory for anisotropic magnetic metamaterials. *Phys. Rev. B* **2009**, *80*, 115101. [[CrossRef](#)]
115. Wang, X.D.; Zhang, X.G.; Yu, Q.L.; Harmon, B.N. Multiple-scattering theory for electromagnetic waves. *Phys. Rev. B* **1993**, *47*, 4161–4167. [[CrossRef](#)]
116. Liu, S.Y.; Lin, Z.F. Opening up complete photonic bandgaps in three-dimensional photonic crystals consisting of biaxial dielectric spheres. *Phys. Rev. E* **2006**, *73*, 066609. [[CrossRef](#)]